RSC Advances

ROYAL SOCIETY OF CHEMISTRY

www.rsc.org/advances

Enhanced Reducibility and Redox Stability of Fe_2O_3 in the Presence of CeO_2 Nanoparticles

Zhenhua Gu,[a, b] *Kongzhai Li,*[b, c]* *Shan Qing,*[b, c] *Xing Zhu,*[b, c] *Yonggang Wei,*[b, c] *Yongtao Li,*[d] *Hua Wang*[b, c]

[a] Oxbridge College, Kunming University of Science and Technology;

[b] State Key Laboratory of Complex Nonferrous Metal Resources Clean Utilization, Kunming University of Science and Technology, Kunming 650093, Yunnan, China;

[c] Faculty of Metallurgical and Energy Engineering, Kunming University of Science and Technology, Kunming 650093, China;

[d] School of Materials Science and Engineering, Anhui University of Technology, Maanshan, 243002,China

*Corresponding author: E-mail address: kongzhai.li@aliyun.com, phone/FAX: 86 871 5153405

Abstract

CeO_2, Fe_2O_3 and a series of CeO_2-modified Fe_2O_3 oxides with different Ce/Fe molar ratios ranging from 5:95 to 50:50 were prepared by a co-precipitation method and thermally aged at different temperatures, which were compared with the corresponding samples prepared by physically mixing CeO_2 and Fe_2O_3. The structural/textural feature, reduction behavior, oxygen storage capacity (OSC), and redox performance of the prepared materials were investigated by XRD, Raman, TEM, BET surface area, XPS, H_2-TPR and oxygen pulse techniques. It is found that CeO_2 particles were very small (<10 nm) and highly dispersed on the surface of Fe_2O_3 rods even after calcination at 800 °C. The nano-size effects resulted in strong chemical interaction in the Fe_2O_3-CeO_2 interfaces, which significantly improved the reducibility of Fe_2O_3 in reducing atmosphere. Hematite-like solid solutions were also observed in the mixed oxides, but it only existed on the materials with relatively low CeO_2 content (Ce/Fe < 20: 80). The formation of hematite-like solid solution could improve the surface reduction of Fe_2O_3, while the deep reduction of Fe_2O_3 depends mainly on the crystal size of Fe_2O_3 particles. The size effect plays a more important role than solid solution on the reduction behavior of CeO_2-modified Fe_2O_3 oxides. In addition, the presence of CeO_2 on Fe_2O_3 also strongly improves the oxygen storage capacity and redox stability of Fe_2O_3, which can be attributed to the chemical interaction between cerium and iron oxides, involving the formation of a complex oxide ($CeFeO_3$) after the TPR/OSC redox testing. This knowledge gives useful references to design novel OSC materials for chemical looping technologies.

1. Introduction

Hematite (α-Fe_2O_3), as a major and thermodynamically most stable oxide among the 16 identified iron oxidic compounds, is one of the most important iron oxides.[1] Because of the high level of reducible ferric iron (Fe(III)), Fe_2O_3-based materials have attracted significant attentions as an oxygen carrier in a novel power generation technology which is named "Chemical-Looping Combustion" (CLC).[2, 3] In this technology, Fe_2O_3 oxygen carriers were submitted to oxidize fuels to H_2O and CO_2, and then the reduced sample can be re-oxidized by air. Because of the separation of fuels from air, this technology is identified as owning inherent advantages for CO_2 separation with minimum energy losses. In addition, Fe_2O_3 was also proposed to be used for hydrogen generation via chemical looping reforming and chemical hydrogen storage.[4-6] Both of the two technologies are performed via the two-step redox reaction of iron oxides. In the process of chemical hydrogen storage, hydrogen firstly reacts with iron oxide to form H_2O (hydrogen storage step), and then hydrogen can be recovered through the oxidation of reduced iron with water vapor (hydrogen release step). In the case of chemical looping reforming, iron oxide is firstly reduced with fuels (e.g., hydrocarbon or syngas) into iron metal or suboxides (reduction step), and then pure hydrogen can be produced through the oxidation of reduced iron with steam.

It was found that the reaction rates of hematite with fuels are slow and this material also has a tendency to deactivate during the redox process at high temperatures. To finalize the successive reduction-oxidation cycles in the above technologies, additives (e.g., NiO) or supports (e.g., Al_2O_3, TiO_2 and $MgAl_2O_4$) were used to improve the reactivity and to overcome deactivation in redox cycles.[2, 7-13] The use of supports could obviously improve the reactivity and redox stability of Fe_2O_3-based oxygen carriers, but it also reduced the amount of reducible oxygen for fuel oxidation. In the case for the additives modified Fe_2O_3 oxygen carriers, carbon deposition can not be neglected

when using hydrocarbons as fuel, because such additives (e.g., reduced Ni species) are usually active for the decomposition of hydrocarbons (e.g., methane). In this case, exploration of a suitable additive which could solve the above questions owns considerable scientific and technological value.[14]

CeO_2 is well known as an oxygen buffer in three way catalyst (TWC) systems due to its outstanding oxygen storage capacity and good redox property.[14-17] CeO_2 also shows excellent resistance to carbon deposition in the partial oxidation of methane.[18, 19] It was reported that using CeO_2 as an additive could improve the catalytic performance of Fe_2O_3-based catalysts by decreasing the particle size,[20] and the formation of CeO_2–doped hematite solid solution could strongly promote the catalytic stability of iron oxides.[21-23] It is reasonable to speculate that combining Fe_2O_3 with CeO_2 may improve the performance of Fe_2O_3 used in a chemical-looping process. Since the chemical-looping processes usually run at relatively high temperatures (≥ 800 °C), the estimation on physicochemical figures such as the reduction behavior, thermal stability and redox property of candidate materials under high-temperature conditions should be performed firstly.

In the present work, a series of CeO_2-modified Fe_2O_3 materials with different Ce/Fe molar ratios was prepared and thermally aged at different temperatures. Based on the structural and chemical characterizations, their structural/textural feature, reduction behavior, oxygen storage capacity (OSC) and redox performance were investigated in detail. The discussions on the results obtained from these studies help us to understand the relationship between the structural properties and the reduction/redox behaviors of CeO_2-modified Fe_2O_3 oxides.

2. Experimental Section

2.1 Material Preparation

CeO_2, Fe_2O_3 and CeO_2-modified Fe_2O_3 oxides with the Ce/Fe mole ratio ranging from 5:95 to 50:50 (labeled as Ce05/Fe95, Ce10/Fe90, Ce20/Fe80, Ce40/Fe60, and Ce50/Fe50, respectively) were prepared by a co–precipitation method. The required amounts of $Ce(NH_4)_2(NO_3)_6$ (Wako, minimum purity 95%) and/or $Fe(NO_3)_3 \cdot 9H_2O$ (Wako, minimum purity 99%) were dissolved in distilled water, and blended using a magnetic stirrer for 30 min at room temperature. The hydroxides were precipitated by dropping an ammonia 8 wt % aqueous solution. The mixtures were stirred for 3 h at the pH of 10. The precipitates were dried at 110 ℃ for 24 h, subjected to decomposition at 600 ℃ in air for 3 h. The Ce20/Fe80-800 sample was prepared by further heat treating the Ce20/Fe80-600 material at 800℃ for 3 h. The

For the preparation of the physically mixed samples, single Fe_2O_3 and CeO_2 precipitates were prepared firstly by a precipitation method in the same operation procedure as above. Both the single Fe_2O_3 and CeO_2 precipitates were calcinated at 600 for 3 h to obtain Fe_2O_3-600 and CeO_2-600 samples. Then, Fe_2O_3-600 and CeO_2-600 powders were mixed with a Ce/Fe mole ratio of 1:4 and grinded for 15 min in an agate mortar. Thereafter, the mixtures were calcinated at 600 ℃ for 1 h to obtain the physically mixed Ce20/Fe80-600 sample. The physically mixed Ce20/Fe80-800 sample was prepared by further heat treating the corresponding Ce20/Fe80-600 material at 800℃ for 3 h.

2.2 Characterization

Powder X-ray diffraction (XRD) patterns were recorded using a Rigaku MiniFlex II diffractometer with Cu Kalpha radiation at 40 kV and 15 mA. The X-ray diffractogram was recorded at scanning rate of 1°/min with a 0.02° step size in the 2θ range between 10 and 80°. Raman spectra were measured with a JASCO (Japan) NRS-3100 Raman Spectrometer, equipped with a TE-cooled charge coupled device (CCD) detector and a green laser (λ=532 nm, frequency-doubled Nd:YVO4, Showa Optronics, Japan), under the ambient atmosphere. The BET surface area was determined by a

volumetric adsorption apparatus by nitrogen adsorption at -196 °C using Micromertics TriStar II. The microstructures and morphologies were investigated using a JEOL JEM-2100(UHR) transmission electron microscope (TEM) at 200 kV.

The X–ray photoelectron spectroscopy (XPS) experiments were carried out on a PHI–5500 system equipped with a monochromatic Mg *K*a X–rays source (*hv*=1253.6 eV). Spectra were registered after purging the samples at ambient temperature in a vacuum (residual pressure<10^{-7} Pa). An electron flood gun compensated sample charging during the measurement. The electron takeoff angle was 45° with respect to the sample surface. The spectra were referenced to the C1s emission at 284.8 eV.

Temperature-programmed reduction (TPR) profiles were obtained from room temperature to 800 °C (hold at 800 °C for 20 min) in a 30 $cm^3 \cdot min^{-1}$ flow of 5% H_2/Ar at a heating rate of 10 °C·min^{-1}. After the TPR cycle, the gas flow was switched to Ar and the sample was cooled down to 600 °C at a cooling rate of 10 °C·min^{-1}. Thereafter, O_2 pulses were injected on the reduced sample at 600 °C, and OSC of this material was obtained by calculating the consumption of oxygen. The redox treatment was performed by repeating TPR/OSC couple steps.

3. Result and discussion

3.1 Interaction between CeO_2 and Fe_2O_3

The combination of Fe_2O_3 with CeO_2 was performed in two ways: co-precipitation and physically mixed methods. Figure 1 shows the XRD patterns of the precipitated Fe_2O_3, co-precipitated CeO_2/Fe_2O_3 samples (with a Ce/Fe mole ratio of 2:8, labelled as Ce20/Fe80) and physically mixed Ce20/Fe80 samples calcined at different temperatures. Table 1 summarized the crystallite sizes and lattice constants of CeO_2 and Fe_2O_3 along with the specific surface area for different samples.

It is shown in Figure 1 that the single Fe_2O_3 samples (Fe_2O_3-600 and Fe_2O_3-800) can be assigned to hematite (α-Fe_2O_3),[24] and the Ce20/Fe80 samples (both physically mixed and co-precipitated samples) displayed mixed reflections from α-Fe_2O_3 and fluorite structured CeO_2 (*Fm*-3*m*). It is clear that higher calcination temperature results in sharper diffraction peaks, indicating the growth of the oxide particles under thermal treatment, especially for the single oxides and the physically mixed sample. A shift of CeO_2 peaks to higher diffraction position was observed over the co-precipitated Ce20/Fe80-600 sample (see the arrow in Figure 1B) compared with the single CeO_2, which coupled with the lattice contraction of CeO_2 (see Table 1) evidences the formation of CeO_2-based solid solution.[23] In addition, a slight expansion in the unit cell of Fe_2O_3, especially in the *c* direction, was also detected in this sample, which can be interpreted as the incorporation of Ce^{4+} into the Fe_2O_3 lattice to form a hematite structured solid solution.[21, 23] When increasing the calcination temperature, the lattice distortion either for CeO_2 or Fe_2O_3 in the co-precipitated Ce20/Fe80 samples disappeared (see Table 1). This indicates that both the two types of solid solution (CeO_2 and hematite-like solid solutions) are unstable under the high-temperature thermal treatment. For the physically mixed samples, the lattice constants determined from Fe_2O_3 and CeO_2 are very close to those of the pure phases, suggesting the absence of solid solution.

Raman analyses for different samples are shown in Figure 2, which supports the XRD finding that the structure of singe Fe_2O_3 is hematite and the mixed oxides contain the mixed phases of hematite and cubic CeO_2.[21, 22] It is clear that the Fe_2O_3-800 sample shows six peaks at approximately 220, 240, 286, 404, 494 and 604 cm^{-1} corresponding to hematite, but two peaks at ca. 240 and 494 cm^{-1}, which are usual visible in very crystalline α-Fe_2O_3, [21] are missing in Fe_2O_3-600 and all the mixed oxides, evidencing small particle size of Fe_2O_3 in such samples.

Noted is that the relative intensity towards the Raman bands of hematite to cubic CeO_2 is very different between co-precipitated and physically mixed samples. For the co-precipitated samples (see Figure 2, curves *e*, *f* and *g*), the hematite features were visible, whereas the Raman band of CeO_2 is very weak. This is in contrast with the Raman spectra of the physically mixed samples (Figure 2 curves *c* and *d*), which show a very observable CeO_2 band with several invisible peaks corresponding to hematite. It was reported that hematite owns strong absorbance at the wavenumber region of the Raman spectrum,[1] which usually results in weaker Raman bands towards iron oxides than CeO_2.[21] This may explain the higher intensity of the Raman features of CeO_2 than that of α–Fe_2O_3 in the physically mixed samples, despite the low molar content of Ce (20%). On the other hand, it is known that the intensity of Raman peaks for CeO_2 is sensitive to its particle size, and bigger crystal size would result in higher intensity of Raman spectra. In this case, the weak Raman band of CeO_2 towards the co-precipitated samples may be attributed to the small size of CeO_2 particles. This is supported by the TEM results in Figure 3.

A red shift (shift toward lower wavenumbers) towards the main band of CeO_2 was also observed in Figure 2 for all the co-precipitated samples compared with the single CeO_2, evidencing the formation of CeO_2-based solid solution.[21] Moreover, a red shift towards the features of Fe_2O_3 was also observed over co-precipitated Ce20/Fe80-600 sample. It was reported that the incorporation of additive ions into the Fe_2O_3 crystal structure could result in a shift of Raman peaks of Fe_2O_3 to lower wavenumbers due to the changes in surface strain and formation of defects.[25] In this case, the red shift of Fe_2O_3 Raman bands may also be attributed to the modification on the surface structure of Fe_2O_3 (e.g., inducing surface strain or defects in hematite like solid solution) due to the presence of CeO_2 particles.

Figure 3 shows the TEM micrographs of coprecipitated Ce20Fe80-800 sample and Ce10/Fe90 sample (which will be discussed in the next section). A rod-like structure with 100-300 nm in length and about 10-35 nm in diameter was observed on both samples, which were closely surrounded by numbers of small particles (5-10 nm). The lattice fringes in the high-resolution TEM micrographs (Figure 6b) indicate that the nanorods and small particles can be identified as CeO_2 and α–Fe_2O_3, respectively. It is worthy to stress that the binding interface between CeO_2 and α–Fe_2O_3 can be observed over both samples, indicating strong structural interaction between the two oxides.

Figure 4 shows the hydrogen reduction behavior of different samples, and the temperature for each reduction peak was represented in Table 2. The TPR profiles of the single Fe_2O_3 samples represented three peaks (α, β and γ), showing a stepwise reduction of Fe_2O_3 to Fe through FeO as an intermediate [24, 26]. All the physically mixed Ce20/Fe80 samples show similar TPR profiles with the single Fe_2O_3, but the co-precipitation samples involves one more reduction peak (δ) below 350 °C (Figure 4, curves *e* and *f*). It has been demonstrated that nanometer sized CeO_2 usually gives a reduction peak under 400 °C,[27] and the formation of CeO_2-based solid solution could reduce the reduction temperature of CeO_2.[14] Taking the observations of the small particle size of CeO_2 (XRD finding) and the formation of surface CeO_2-based solid solution (Raman finding) into account, we ascribed the δ peak to the reduction of surface CeO_2.

It is very interesting that the physically mixed Ce20/Fe80-600 sample (Figure 4, curve *c*) shows a lower temperature of α peak compared with Fe_2O_3-600, although no obvious structural interaction was detected by the XRD or Raman characterization (Figures 1 and 2). This indicates that even simple contact between CeO_2 and Fe_2O_3 may improve the surface reducibility of Fe_2O_3 in the CeO_2-Fe_2O_3 mixed oxides. On the other hand, the temperatures for β and γ peaks towards co-precipitated Ce20/Fe80-600 sample were lower (Figure 4, curve *e*) than that towards Fe_2O_3-600

(Figure 4, curve *a*) or the physically mixed Ce20/Fe80-600 sample (Figure 2, curve *c*), indicating relatively higher reducibility. This should be related to the structural interactions (e.g., the formation of CeO_2-Fe_2O_3 interface and solid solution) occurred in the co-precipitated Ce20/Fe80-600 sample.

With the increase of the calcination temperature from 600 to 800 °C, the temperature of α peak shifted to higher temperature with respect to the single Fe_2O_3 (Figure 4, curve *a* and *b*) and physically mixed samples (Figure 4, curve *c* and *d*). By contrast, no obvious changes were observed on the α peak for the two co-precipitation samples (Figure 4, curves *e* and *f*), suggesting higher stability for the reducibility under thermal treatment. It should be stressed that co-precipitated Ce20/Fe80-600 sample owns both the ceria-like and hematite-like solid solution, but both of them disappeared when increasing calcination temperature from 600 to 800 °C (XRD observation). The similar reduction behaviors between co-precipitated Ce20/Fe80-600 and Ce20/Fe80-800 samples indicate that the solid solution may not be a determining factor for the reducibility of such CeO_2-Fe_2O_3 materials.

In summary, the comparison between co-precipitated and physically mixed Ce20/Fe80 samples indicates that physical contact between CeO_2 and Fe_2O_3 oxides could improve the surface reducibility of Fe_2O_3, and the chemical interaction in the Fe_2O_3-CeO_2 interfaces could improve both the surface and bulk reducibility of Fe_2O_3.

3.2 Effect of CeO_2 contents

As the above suggestions, the co-precipitated CeO_2/Fe_2O_3 oxides show obvious structural and chemical Ce-Fe interaction. A series of CeO_2-modified Fe_2O_3 oxides with the Ce/Fe mole ratio ranging from 5:95 to 50:50 were therefore prepared by the co-precipitation method. The XRD patterns of CeO_2, Fe_2O_3 and CeO_2-modified Fe_2O_3 oxides with different CeO_2 contents calcined at

800 °C were shown in Figure 5. The single CeO_2 diffractogram was characteristic of a cubic fluorite-structured material (*Fm*-3*m*) [17] and all the diffraction peaks for pure Fe_2O_3 was attributed to α–Fe_2O_3.[24] The mixed samples displayed reflections from both phases, but all the diffraction peaks for each phase broadened and weakened compared with the single oxides, evidencing smaller size of particles in the mixed oxides. This can be confirmed by the calculated crystal sizes (based on the XRD data) of Fe_2O_3 and CeO_2, as shown in Table 3.

It can also be observed from Figure 5 (B) that the diffraction of (110) plane owning to α–Fe_2O_3 shifted to lower 2θ position when increasing the Ce content from 5% to 10%. Moreover, the lattice constants of hematite detected in the two samples (Ce05/Fe95 and Ce10/Fe90) were also found larger than those towards the single Fe_2O_3 (see Table 3). This lattice expansion must be due to the incorporation of larger Ce^{4+} into the hematite lattice, evidencing the formation of a hematite-like solid solution.[21-23] When further increasing the Ce content, *a* and *c* of the α–Fe_2O_3 parameters changed backed to those of pure hematite, as shown in Table 3, which indicates the disappearance of the hematite-like solid solution in the Ce-Fe material with relatively high CeO_2 content (≥20% mole content). On the other hand, the lattice constant of CeO_2 (not shown) from all the mixed oxides is very close to that of the single CeO_2, suggesting no CeO_2-based solid solution in these samples.

The contents of CeO_2 also affect the specific surface area of the mixed oxides. Since the thermal treatment temperature is as high as 800 °C, the specific surface area either for single CeO_2 or Fe_2O_3 is very low (lower than 3 $m^2 \cdot g^{-1}$, see Table 3). But it increased to ca. 20 $m^2 \cdot g^{-1}$ when combining Fe_2O_3 with CeO_2. It should be noted that when the content of Ce is higher than 20%, the specific surface area slightly decreased with CeO_2 content. This suggests that there is a critical content of CeO_2 for obtaining relatively high surface area toward the CeO_2-modified Fe_2O_3 materials, which

may be attributed to the absence of hematite-like solid solution in the samples with relatively high loading of CeO_2 (Ce/Fe > 20: 80).

The Raman spectra for the prepared samples are shown in Figure 6. The single CeO_2 exhibits a prominent band at 466 cm^{-1} corresponding to F_{2g} Raman active mode in metal dioxides with a fluorite–like structure, and six bands at approximately 220, 240, 286, 404, 494 and 604 cm^{-1} corresponding to α–Fe_2O_3 were observed over the single Fe_2O_3 sample.[21] The mixed oxides show the Raman bands owning to both CeO_2 and α–Fe_2O_3 phases, but the full width at half maximum (FWHM) for each band is wider than that towards the single oxides. It is also clear that two weak peaks at ca. 240 and 494 cm^{-1}, which are visible in single Fe_2O_3, are missing in all the mixed oxides. The disappearance of these Raman bands is characteristic of Fe_2O_3 with low crystallite size. [21]

It should be noted that the band for CeO_2 in the mixed oxides is much weaker and wider than that towards the single CeO_2 and shifts to lower frequency (see the arrow in Figure 6). It is generally accepted that the broadening of the ceria main line is related either to a decrease of ceria crystallite size or to the presence of defects such as oxygen vacancies,[28] and the red shift of ceria band is a sign of lattice contraction due to the cation doping.[29] The above phenomena suggest the formation of CeO_2-based solid solution due to the incorporation of Fe^{3+} into the CeO_2 lattice. This is inconsistent with the XRD finding that no ceria-based solid solution in the mixed oxides. Since the Raman spectra are only sensitive to the information of materials surface, the modified CeO_2 should exist only in the surface layer of the mixed oxides.

Figure 7 shows the TPR profiles of single CeO_2, Fe_2O_3 and CeO_2-modified Fe_2O_3 oxides. As discussed in Figure 4, the TPR profiles for all the samples show three main peaks (α, β and γ) which evidence the stepwise reduction of Fe_2O_3 to Fe and one small shoulder peak (δ), relating to the reduction of surface CeO_2 particles. The α peak shifted to lower temperatures due to the addition of

CeO_2, but the degree of this shift decreased when the CeO_2 content is higher than 20%. On the other hand, the temperature of β peak for the Ce05/Fe95 and Ce10/Fe90 samples is same with that towards the single Fe_2O_3, but further increasing the CeO_2 content resulted in an obvious decrease in the temperature of this peak. It was observed from the XRD characterization that addition of small amount of CeO_2 (Ce/Fe < 20: 80) into Fe_2O_3 would lead to the formation of hematite-like solid solution, while the samples with high CeO_2 content (Ce/Fe ≥ 20: 80) owns smaller Fe_2O_3 particles. As discussed above, the α and β peaks are attributed to the reduction of surface Fe^{3+} and the further reduction of subsurface Fe^{3+} and surface Fe^{2+}, respectively.[24] In this case, the shift of α peak indicates that the formation of hematite-like solid solution may improve the surface reduction of Fe_2O_3. The shift of β peak suggests that the deep reduction of Fe_2O_3 is more sensitive to the crystal size of Fe_2O_3 particles, because smaller particles would shorten the distance for oxygen migration from the bulk to surface. Another important feature in Figure 7 is the shifts of δ peak to higher temperature with the content of CeO_2. Since the reduction temperature of CeO_2 particles is very sensitive to the particle size, this should be due to the increased crystal size of CeO_2 particles for the samples with higher loading of CeO_2 (see Table 3).

To summarise, the characterizations of CeO_2, Fe_2O_3 and CeO_2-modified Fe_2O_3 oxides suggest that the coprecipitation protocol allowed Fe_2O_3-CeO_2 mixed oxides own smaller particle size and bigger specific surface area, diminishing thermal sintering at high temperature. These modifications enhanced the reducibility of CeO_2 and Fe_2O_3 in the mixed oxides, especially for the sample with a suitable content of CeO_2 (e.g., Ce20/Fe80 sample).

3.3 Redox property of CeO_2-modified Fe_2O_3

For a chemical-looping process, the redox property of oxygen carriers is one of the most important factors for practical application. The redox property of CeO_2-modified Fe_2O_3 was investigated by alternately carrying out the H_2-TPR characterization and oxygen storage capacity (OSC) measurements. Figure 8 compares the TPR profiles of the Fe_2O_3 and co-precipitated Ce20/Fe80-800 samples before and after redox cycles.

It can be seen that the TPR behavior of recycled Fe_2O_3 is substantially different from that exhibited by the fresh sample (Figure 8A). When the redox treatment was performed for once, all the reduction peaks (Figure 8A, cycle 1) lost a bit of their intensity, especially for the high-temperature peaks. Further increasing the cycle number modified the TPR profile to reach a final appearance with only one weak peak at ca. 505 °C (Figure 8A, cycle 6). After six redox cycles, the OSC of the single Fe_2O_3 sample decreased from 0.67 mmol/g to 0.20 mmol/g (see Figure 9), indicating that over 70% of oxygen species in single Fe_2O_3 consumed in the TPR process cannot be restored in the re-oxidation step (OSC step).

A totally different and in some respects interesting behavior pattern is observed over the recycled Ce20/Fe80 sample (Figure 8B). It is clear that the first low-temperature peak weakened, but the bulk reduction which occurs at high-temperature (600-800°C) was gradually enhanced with the redox cycle. As a result, the OSC of this sample significantly increased from 1.57 to 2.1 mmol/g after six redox cycles, as shown in Figure 9.

All these modifications on the reduction behavior and OSC towards the Ce20/Fe80 sample can be correlated to the phase changes of these materials during the redox treatment. Figure 10 compares the XRD patterns of Fe_2O_3 and Ce20/Fe80 samples before and after redox cycling. It can be seen that, after re-oxidation step, the diffractions of Fe_2O_3 disappeared, and suboxides of iron (i.e., Fe_3O_4, FeO) and Fe phases were observed (Figure 10A, cycle 1). Further recycling of the sample still

modifies the XRD pattern: the relatively intensity ratio of the diffractions of FeO and Fe to Fe_3O_4 obviously increased (from cycles 1 to 6 in Figure 10A). This indicates that the only reduction peak in the TPR of the recycled single Fe_2O_3 sample in Figure 8A is attributed to the reduction of Fe^{2+}. It can also be used to explain the decreased OSC of the single Fe_2O_3 after successive redox cycling, as shown in Figure 9.

The redox treatment also modified the composition of the Ce20/Fe80 sample (Figure 10B). Similarly with the recycled single Fe_2O_3 sample, diffractions from Fe_3O_4 and Fe were observed on the Ce20/Fe80 sample after the first TPR/OSC redox cycle. However, it should highlight that α-Fe_2O_3 was also detected on this sample, which contrasts with the fact that no Fe^{3+} was found to appear in the recycled single Fe_2O_3 sample, suggesting that more oxygen species were restored in the re-oxidation step due to the presence of CeO_2. This phenomenon gives the reason why Ce20/Fe80 sample owns higher OSC value than the single Fe_2O_3 after the redox treatment. It also should be noted that further redox cycling slightly improved the relative intensity of the diffractions from α-Fe_2O_3 to other phases (Figure 10B, cycles 1 to 6), evidencing the increased content of α-Fe_2O_3 in this material. This is in accordance with the improvement on the OSC of Ce20/Fe80 sample after the successive redox cycling (see Figure 9).

Another interesting finding due to the combination of CeO_2 and Fe_2O_3 is the formation of $CeFeO_3$ in the recycled Ce20/Fe80 sample. It was reported that cerium orthoferrite ($CeFeO_3$) can be prepared by the reaction $3CeO_2 + Fe_2O_3 + Fe \rightarrow 3CeFeO_3$ in inert atmosphere.[30] In the present work, the formation of $CeFeO_3$ should also follow the same route because of the coexistence of CeO_2, Fe_2O_3 and Fe phases. To investigate the redox property of $CeFeO_3$, pure $CeFeO_3$ was prepared with a calcination temperature of 800 °C. It is found that the $CeFeO_3$ is unstable in the TPR/OSC redox process. After six redox cycles, most of the $CeFeO_3$ decomposed to Fe_2O_3 and CeO_2 (see Figure S1).

It should be mentioned that $CeFeO_3$ is very stable in the CH_4/H_2O redox atmosphere.[31, 32] This indicates that above mentioned decomposition of $CeFeO_3$ should occur in oxygen atmosphere of OSC measurement step. However, in the present work, the repetitive redox cycles did not reduce the intensity of the diffraction peaks of $CeFeO_3$ during the redox processes, indicating that the structure of $CeFeO_3$ in the recycled Ce20/Fe80 sample is highly stable under redox treatment. This may be attributed to the co-existence of CeO_2, Fe_2O_3, Fe and $CeFeO_3$ in this sample, which could result in a dynamic balance between the formation and decomposition of $CeFeO_3$ in the redox atmospheres.

It is generally accepted that exposed Ce^{3+} ions on CeO_2-based materials could improve the rate of many chemical reactions, because adsorbed gases or catalytic reaction intermediates can interact simultaneously with several Ce^{3+} ions.[33] XPS measurement on the $CeFeO_3$ revealed a pair of new bands at ca. 886.5 (V') and 902.6 eV (U') with very high intensity compared with the single CeO_2, evidencing high concentration of Ce^{3+} ions on this material (Figure S2). In this case, the $CeFeO_3$ with abundant Ce^{3+} ions may act as a catalyst to improve the reducibility of Ce and Fe oxides in the recycled Ce20/Fe80 sample through activating hydrogen and lattice oxygen in the TPR process. That is to say, the formation of $CeFeO_3$ in the CeO_2-Fe_2O_3 system may be a key to maintain a relative high reducibility and oxygen storage capacity in the repeated reduction/oxidation cycle.

Figure 11 reveals the Raman spectra of Ce20/Fe80 before and after redox treatment, which give more information on the surface iron species. Fe_3O_4 and Fe, which is detected in the XRD measurement (Figure 10), cannot be observed by Raman spectra (Figure 11, cycles 1 and 6). This should be attributed to the low content of Fe_3O_4 and the extremely low sensitivity of Raman to metals. It should be noted that the Raman bands corresponding to α-Fe_2O_3 broadened, weakened and shifted to lower wavenumbers after redox cycles. These phenomena evidence the decrease of α-Fe_2O_3 particle size and the presence of surface strain or defects on the surface of recycled

Ce20/Fe80 sample. This may also be a possible contribution to the relatively high reducibility of Ce20/Fe80 material after the successive redox treatments. Beyond this, a red shift towards the Raman band of CeO_2 (Figure 11, cycles 1 and 6) was also detected in the recycled Ce20/Fe80 sample, indicating the lattice distortion of cerium oxide due to existence of Ce^{3+}.[30] This can be related to the presence of $CeFeO_3$, which owns abundant Ce^{3+} ions, as observed by XPS measurement (Figure S2).

The above results indicate that the presence of CeO_2 on Fe_2O_3 could improve the oxygen storage capacity and redox stability of Fe_2O_3 due to strong chemical interactions between cerium and iron oxides, involving the formation of a complex oxide ($CeFeO_3$).

4. Conclusions

The modification of CeO_2 (with different loadings) on the structure, reduction behavior, OSC and redox property of Fe_2O_3 was investigated. Incorporation of Fe_2O_3 with CeO_2 using a co-precipitation method reduced the crystal size of both oxides and increased the specific surface area, diminishing thermal sintering at high temperature. TEM images shows that CeO_2 particles were very small (<10 nm) and highly dispersed on the surface of Fe_2O_3 rods, even after high-temperature treatment. This suggests that the Fe_2O_3 rods as support could inhibit the growth CeO_2 nano particles under thermal treatment. The nano-size effects resulted in strong chemical interaction in the Fe_2O_3-CeO_2 interfaces, which could improve the reducibility of cerium and iron oxides both on the surface and in the bulk. The physically mixed samples showed that even simple contact between CeO_2 and Fe_2O_3 oxides could improve the reducibility of Fe_2O_3, but this enhancement was restricted to surface reduction behavior.

The presence of CeO_2 could also improve the reversibility of Fe_2O_3 in the successive reduction/oxidation testing, which resulted in a significant improvement on the OSC of the mixed oxide compared with the single Fe_2O_3. The improved redox property of CeO_2-modified Fe_2O_3 sample seems to be related with the formation of perovskite-type $CeFeO_3$ after the redox treatments. It should be stressed that the recycled CeO_2-modified Fe_2O_3 oxides own good reducibility only at high-temperature, indicting this material could potentially be valuable in the redox process occurred at high temperature, such as the chemical-looping technologies.

Acknowledgements

Financial supported from the National Natural Science Foundation of China (Project Nos. 51374004, 51204083, 51104074 and 51174105).

Notes and references

1 R. M. Cornell and U Schwertmann, The iron oxides: structure, properties, reactions, occurrence, and uses. Wiley-VCH: Weinheim 2003.

2 M. M. Hossain and H. I. de Lasa, *Chem. Eng. Sci.,* 2008**, 63**, 4433-4451.

3 J. Adanez, A.Abad, F. Garcia-Labiano, P. Gayan and L. F. de Diego, *Prog. Energy Combust. Sci.,* 2012**, 38**, 215-282.

4 S. Takenaka, V. T. D. Son, C. Yamada and K. Otsuka, *Chem. Lett.,* 2003**, 32**, 1022-1023.

5 K. Otsuka, C.Yamada, T. Kaburagi and S. Takenaka, *Int. J. Hydrogen Energy***,** 2003**, 28**, 335-342.

6 M. A. Gondal, A. Hameed, Z. H. Yamani and A. Suwaiyan, *Appl. Catal., A,* 2004**, 268**, 159-167.

7 M.Johansson, T. Mattisson and A. Lyngfelt, *Ind. Eng. Chem. Res.,* 2004**, 43**, 6978-6987.

8 S. Takenaka, T. Kaburagi, C. Yamada, K. Nomura and K. Otsuka, *J. Catal.,* 2004**, 228**, 66-74.

9 S. Takenaka, N. Hanaizumi, V. T. D. Son and K. Otsuka, *J. Catal.,* 2004**, 228**,, 405-416.

10 J. C. Ryu, D. H. Lee, K. S. Kang, C. S. Park, J. W. Kim and Y. H. Kim, *J. Ind. Eng. Chem.,* 2008**, 14**, 252-260.

11 M. Ryden, E. Cleverstam, M. Johansson, A. Lyngfelt and T. Mattisson, *AlChE J.,* 2010**, 56**, 2211-2220.

12 S. Y. Chen, Q. L. Shi, Z. P. Xue, X. Y. Sun and W. G. Xiang, *Int. J. Hydrogen Energy,* 2011**, 36**, 8915-8926.

13 H. Wang, X. J. Liu and F. Wen, *Int. J. Hydrogen Energy,* 2012**, 37**, 977-983.

14 A. Trovarelli, *Catal. Rev.,* 1996**, 38**, 439-520.

15 M. J. Ozawa, Alloys Compd., 1998, **275–277**, 886-890.

16 C. Larese, M. L. Granados, F. C. Galisteo, R. Mariscal and J. L. G. Fierro, *Appl. Catal., B,* 2006, **62**, 132-143.

17 P. Munusamy, S. Sanghavi, T. Varga and T. Suntharampillai, *RSC Adv.*, 2014,**4**, 8421.

18 T. L. Zhu and M. Flytzani-Stephanopoulos, *Appl. Catal., A,* 2001**, 208**, 403-417.

19 F. B. Passos, E. R. de Oliveira, L. V. Mattos and F. B. Noronha, *Catal. Today,* 2005**, 101**, 23-30.

20 Y. Liu and D. Z. Sun, *J. Hazard. Mater.,* 2007**, 143**, 448-454.

21 F. J. Perez-Alonso, M. L. Granados, M. Ojeda, P. Terreros, S. Rojas, T. Herranz, J. L. G. Fierro, M. Gracia, and J. R. Gancedo, *Chem.Mater.,* 2005**, 17**, 2329-2339.

22 F. J. Perez-Alonso, M. L. Granados, M. Ojeda, T. Herranz, S. Rojas, P. Terreros, J. L. G. Fierro, M. Gracia, J. R. Gancedo, *J. Phys. Chem. B,* 2006**, 110**, 23870-23880.

23 F. J. Perez-Alonso, I. Melian-Cabrera, M. L. Granados, F. Kapteijn and J. L. G. Fierro, *J. Catal.,* 2006**, 239**, 340-346.

24 J. Zielinski, I. Zglinicka, L. Znak and Z. Kaszkur, *Appl. Catal., A,* 2010**, 381**, 191-196.

25 G. Litt and C. Almquist, *Appl. Catal. B,* 2009**, 90**, 10-17.

26 G. Magnacca, G. Cerrato, C. Morterra, M. Signoretto, F. Somma and F. Pinna, *Chem. Mater.,* 2003**, 15**, 675-687.

27 K. Zhou, X. Wang, X. Sun, Q. Peng and Y. Li, *J. Catal.,* 2005**, 229**, 206-212.

28 L. Ilieva, G. Pantaleo, J. W. Sobczakc, I. Ivanov, A. M. Venezia and D. Andreeva, *Appl. Catal., B,* 2007**, 76**, 107-114.

29 G. S. Li, R. L. Smith and H. Inomata, *J. Amer. Chem. Soc.,* 2001, **123**, 11091-11092.

30 M. Robbins, G. K. Wertheim, A. Menth and R. C. Sherwood, J. Phys. Chem. Solids, **1969**, 30, 1823-1825.

31 X. Zhu, H. Wang, Y. G. Wei, K. Z. Li, X. M. Cheng, J. Rare Earths, 2010, **28**, 907-913.

32 F. Mahmoodi, S. H. Najibi, A. Shariati, J. Am. Sci., 2012, **8**,453-459

33 C. T. Campbell and C. H. F. Peden, *Science* 2005**, 309**, 713-714.

Table captions

Table 1. Structural characterizations of Fe_2O_3, physically mixed and co-precipitated Ce20/Fe80 samples with different calcination temperatures.

Table 2. Temperatures of the TPR peaks in Figure 4.

Table 3. Structural characterizations of Fe_2O_3, CeO_2, CeO_2-modified Fe_2O_3 oxides.

Table 1. Structural characterizations of Fe_2O_3, physically mixed and co-precipitated Ce20/Fe80 samples with different calcination temperatures.

Samples	Crystallite size (nm)		Lattice constant of Fe_2O_3 (nm)			S_{BET} ($m^2 \cdot g^{-1}$)
	CeO_2	Fe_2O_3	CeO_2	Fe_2O_3		
				a	c	
Fe_2O_3-600	--	38.6	--	0.5035 ±0.0001	1.3739 ±0.0002	8.3
Fe_2O_3-800	--	71.1	--	0.5031 ±0.0001	1.3741 ±0.0001	2.7
PM-600	18.5	39.5	0.5410 ±0.0002	0.5034 ±0.0005	1.3736 ±0.0003	13.2
PM-800	56.5	69.7	0.5412 ±0.0001	0.5032 ±0.0002	1.3740 ±0.0003	2.5
CP-600	6.6	5.4	0.5378 ±0.0004	0.5029 ±0.0005	1.3825 ±0.0009	51.2
CP-800	13.2	10.2	0.5408 ±0.0001	0.5040 ±0.0002	1.3772 ±0.0006	23.9

S_{BET}: specific surface area; PM: physically mixed Ce20/Fe80; CP: co-precipitated Ce20/Fe80

Table 2. Temperatures of the TPR peaks in Figure 4.

Sample	Temperature of TPR peaks / °C			
	δ	α	β	γ
Fe_2O_3-600	--	438	719	800
Fe_2O_3-800	--	456	676	800
PM-600	--	421	680	800
PM-800	--	443	691	800
CP-600	343	435	611	790
CP-800	335	440	629	800

Table 3. Structural characterizations of Fe_2O_3, CeO_2 and CeO_2-modified Fe_2O_3 oxides.

Samples	Crystallite size (nm)		Lattice constant of Fe_2O_3 (nm)		S_{BET}
	CeO_2	Fe_2O_3	*a*	*c*	($m^2 \cdot g^{-1}$)
Fe_2O_3	--	71.1	0.5031±0.0001	1.3741±0.0001	2.7
Ce05/Fe95	11.5	32.7	0.5040±0.0002	1.3812±0.0002	19.7
Ce10/Fe90	10.3	31.8	0.5045±0.0002	1.3838±0.0003	24.2
Ce20/Fe80	13.2	30.6	0.5040±0.0002	1.3772±0.0006	23.9
Ce40/Fe60	20.2	23.3	0.5030±0.0003	1.3761±0.0002	18.5
Ce50/Fe50	20.1	10.8	0.5032±0.0004	1.3766±0.0003	13.8
CeO_2	58.7	--	--	--	2.2

S_{BET}: specific surface area

Figure captions

Figure 1. (A) XRD patterns of Fe_2O_3, physically mixed and co-precipitated Ce20/Fe80 samples with different calcination temperatures: (a) Fe_2O_3-600, (b) Fe_2O_3-800, (c) physically mixed Ce20/Fe80-600, (d) physically mixed Ce20/Fe80-800, (e) co-precipitated Ce20/Fe80-600, and (f) co-precipitated Ce20/Fe80-800; (B) amplification of the (111) reflection for CeO_2.

Figure 2. Raman spectra of Fe_2O_3, physically mixed and co-precipitated Ce20/Fe80 samples with different calcination temperatures: (a) Fe_2O_3-600, (b) Fe_2O_3-800, (c) physically mixed Ce20/Fe80-600, (d) physically mixed Ce20/Fe80-800, (e) co-precipitated Ce20/Fe80-600, and (f) co-precipitated Ce20/Fe80-800

Figure 3. TEM and HRTEM micrographs of Ce10/Fe90 (a and b) and co-precipitated Ce20/Fe80-800 (c and d) samples.

Figure 4. TPR profiles of Fe_2O_3, physically mixed and co-precipitated Ce20/Fe80 samples with different calcination temperatures: (a) Fe_2O_3-600, (b) Fe_2O_3-800, (c) physically mixed Ce20/Fe80-600, (d) physically mixed Ce20/Fe80-800, (e) co-precipitated Ce20/Fe80-600, and (f) co-precipitated Ce20/Fe80-800

Figure 5. (A) XRD patterns of CeO_2, Fe_2O_3 and CeO_2-modified Fe_2O_3 oxides; (B) Amplification of the (110) reflection for α-Fe_2O_3.

Figure 6. Raman spectra of of CeO_2, Fe_2O_3 and CeO_2-modified Fe_2O_3 oxides.

Figure 7. TPR profiles of CeO_2/Fe_2O_3 mixed oxides calcinated at 800 °C: (a) Ce50/Fe50, (b) Ce40/Fe60, (c) Ce20/Fe80, (d) Ce10/Fe90, (e) Ce05/Fe95, (f) Fe_2O_3

Figure 8. Effect of redox treatment on the reduction behaviors of Fe_2O_3 (A) and Ce20/Fe80 sample (B).

Figure 9 Effect of redox treatment on the OSC of Fe_2O_3 and Ce20/Fe80 sample.

Figure 10. Effect of redox treatment on the XRD patterns of Fe_2O_3 (A) and Ce20/Fe80 sample (B).

Figure 11. Effect of redox treatment on the Raman spectra of Ce20/Fe80 sample.

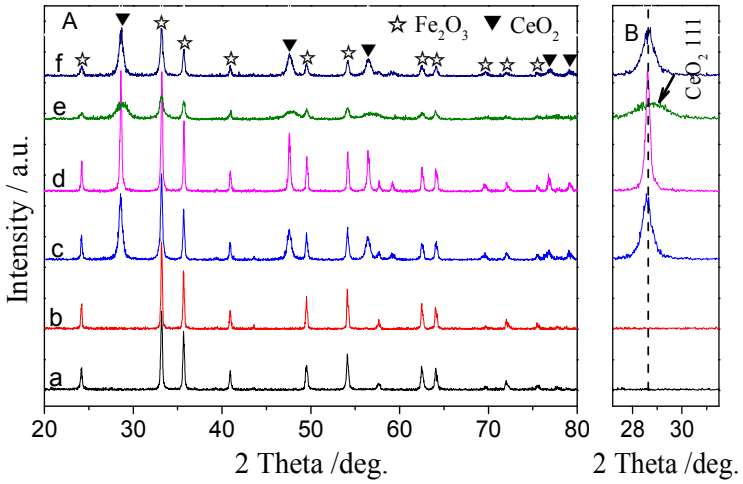

Figure 1. (A) XRD patterns of Fe_2O_3, physically mixed and co-precipitated Ce20/Fe80 samples with different calcination temperatures: (a) Fe_2O_3-600, (b) Fe_2O_3-800, (c) physically mixed Ce20/Fe80-600, (d) physically mixed Ce20/Fe80-800, (e) co-precipitated Ce20/Fe80-600, and (f) co-precipitated Ce20/Fe80-800; (B) amplification of the (111) reflection for CeO_2.

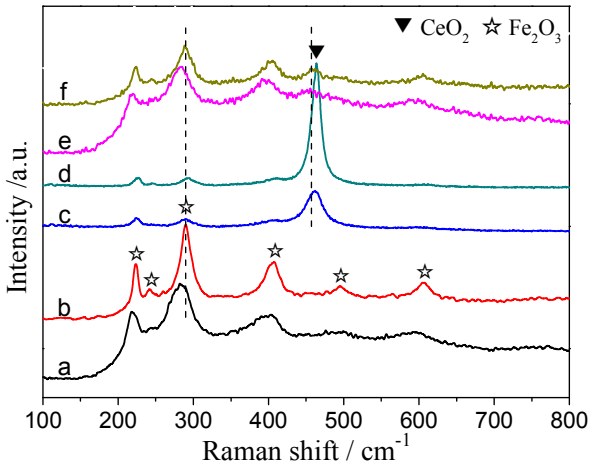

Figure 2. Raman spectra of Fe_2O_3, physically mixed and co-precipitated Ce20/Fe80 samples with different calcination temperatures: (a) Fe_2O_3-600, (b) Fe_2O_3-800, (c) physically mixed Ce20/Fe80-600, (d) physically mixed Ce20/Fe80-800, (e) co-precipitated Ce20/Fe80-600, and (f) co-precipitated Ce20/Fe80-800

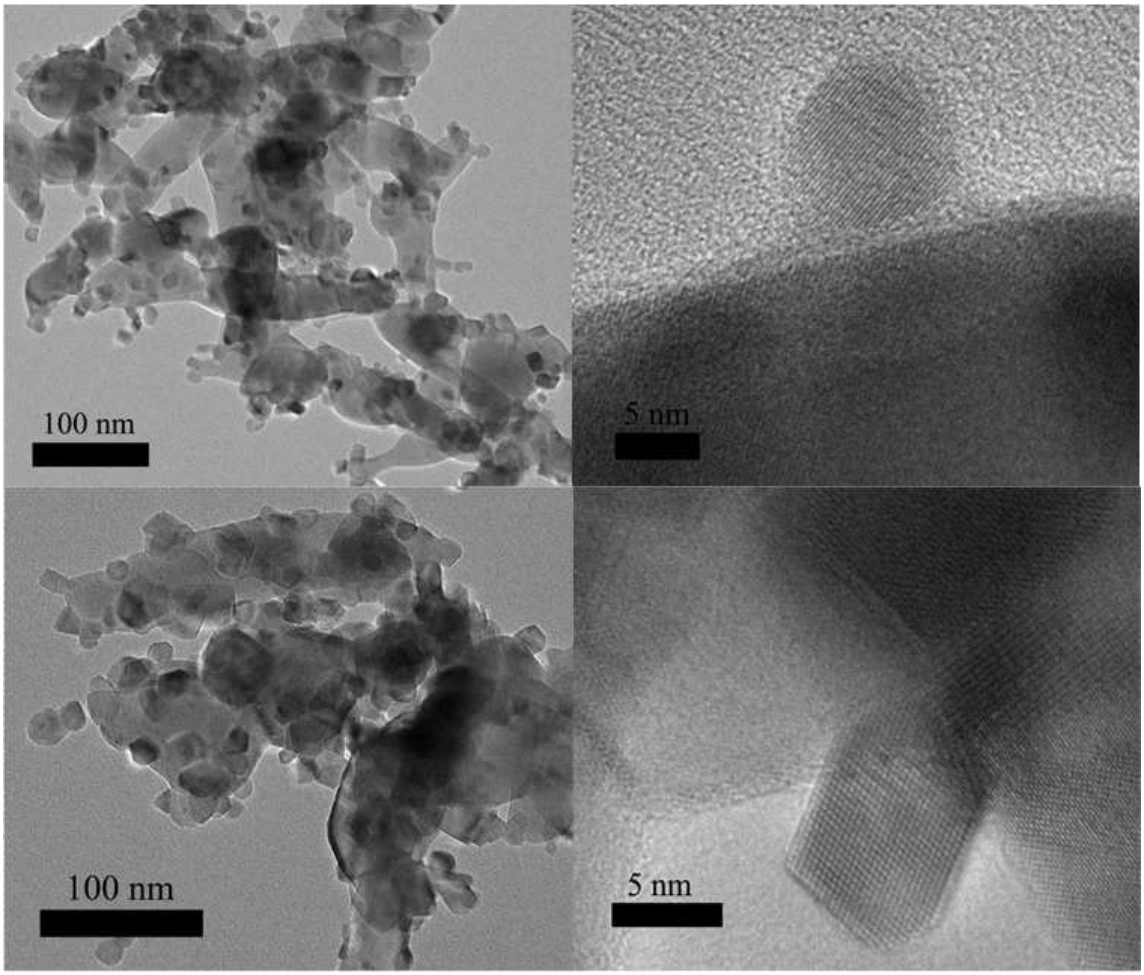

Figure 3. TEM and HRTEM micrographs of Ce10/Fe90 (a and b) and co-precipitated Ce20/Fe80-800 (c and d) samples.

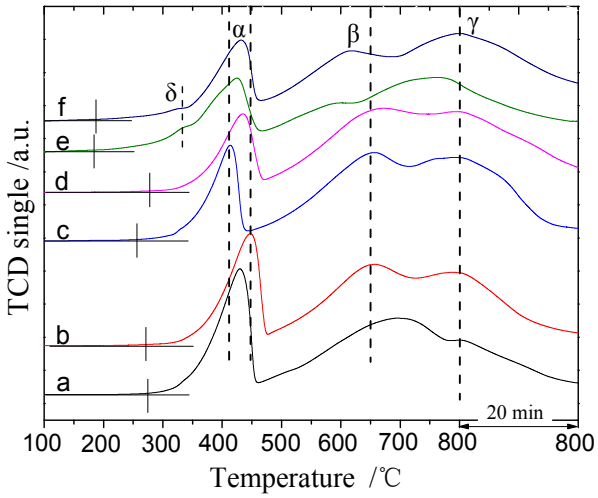

Figure 4. TPR profiles of Fe_2O_3, physically mixed and co-precipitated Ce20/Fe80 samples with different calcination temperatures: (a) Fe_2O_3-600, (b) Fe_2O_3-800, (c) physically mixed Ce20/Fe80-600, (d) physically mixed Ce20/Fe80-800, (e) co-precipitated Ce20/Fe80-600, and (f) co-precipitated Ce20/Fe80-800

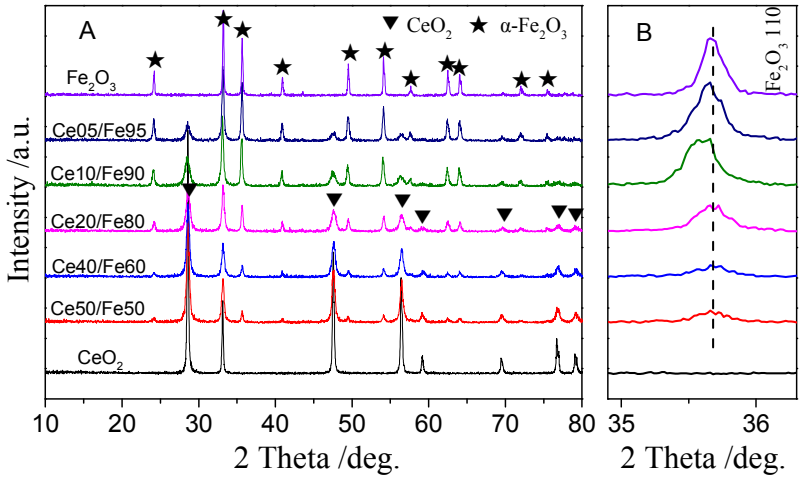

Figure 5. (A) XRD patterns of CeO_2, Fe_2O_3 and CeO_2-modified Fe_2O_3 oxides; (B) Amplification of the (110) reflection for α-Fe_2O_3.

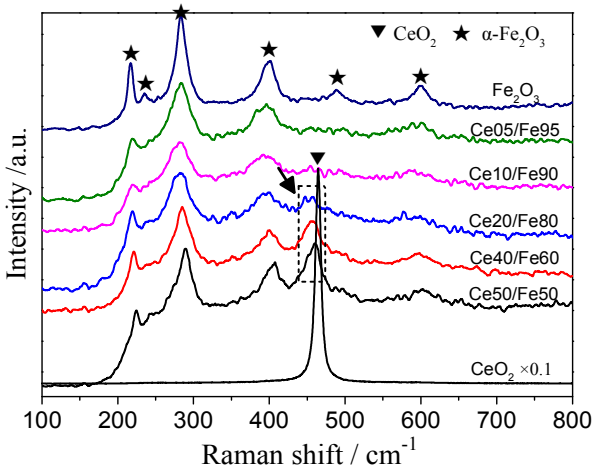

Figure 6. Raman spectra of of CeO_2, Fe_2O_3 and CeO_2-modified Fe_2O_3 oxides.

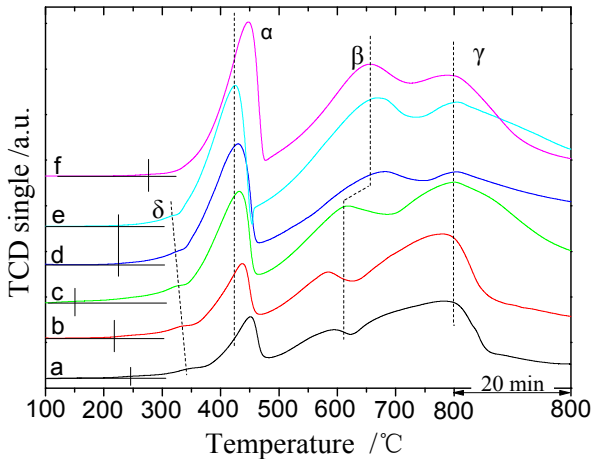

Figure 7. TPR profiles of CeO_2/Fe_2O_3 mixed oxides calcinated at 800 °C: (a) Ce50/Fe50, (b) Ce40/Fe60, (c) Ce20/Fe80, (d) Ce10/Fe90, (e) Ce05/Fe95, (f) Fe_2O_3

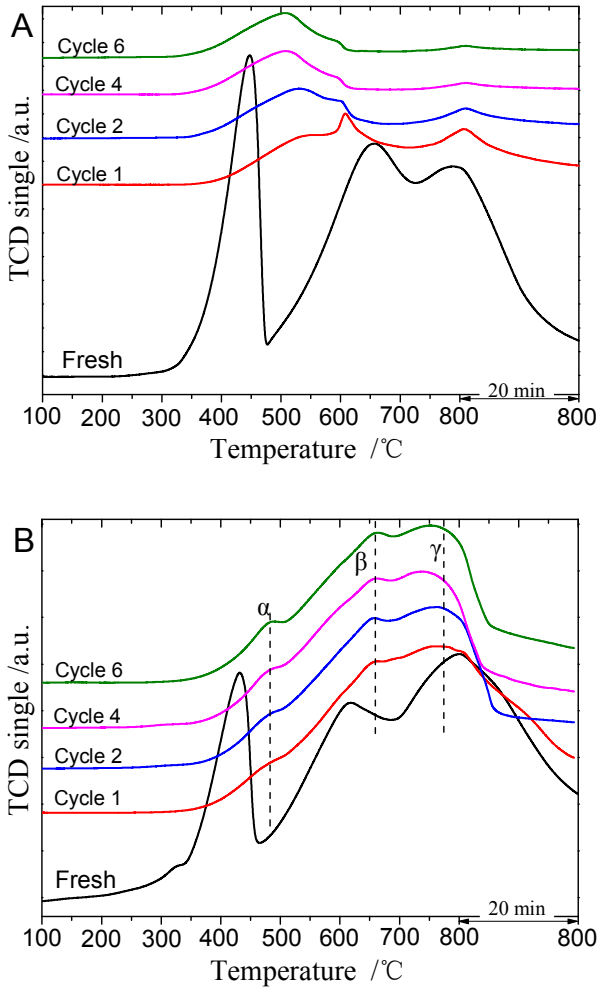

Figure 8. Effect of redox treatment on the reduction behaviors of Fe_2O_3 (A) and Ce20/Fe80 sample (B).

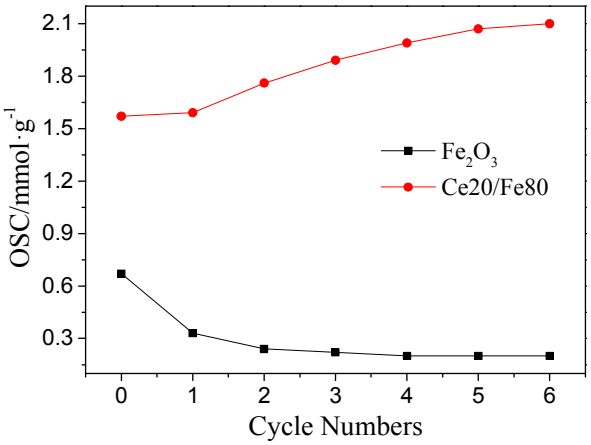

Figure 9 Effect of redox treatment on the OSC of Fe_2O_3 and Ce20/Fe80 sample.

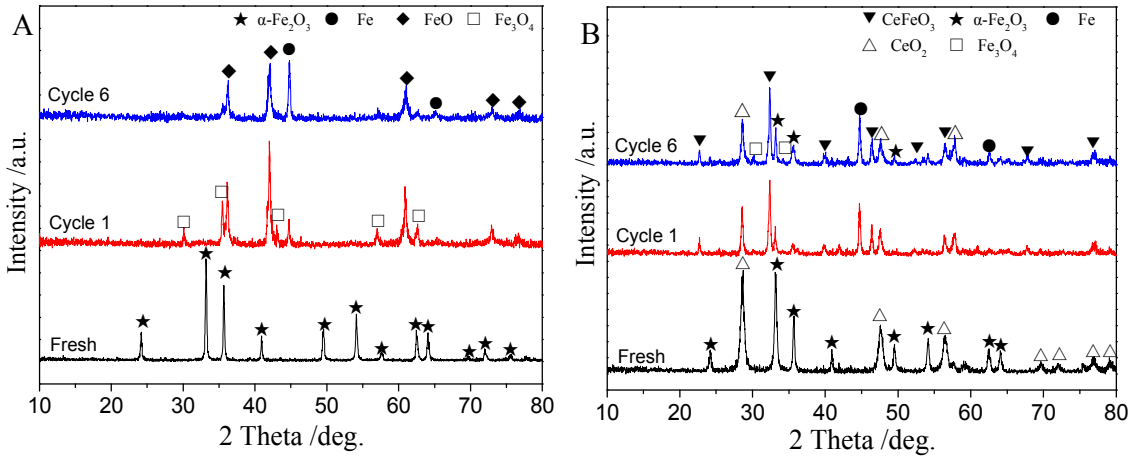

Figure 10. Effect of redox treatment on the XRD (A) patterns of Fe_2O_3 and Ce20/Fe80 sample (B).

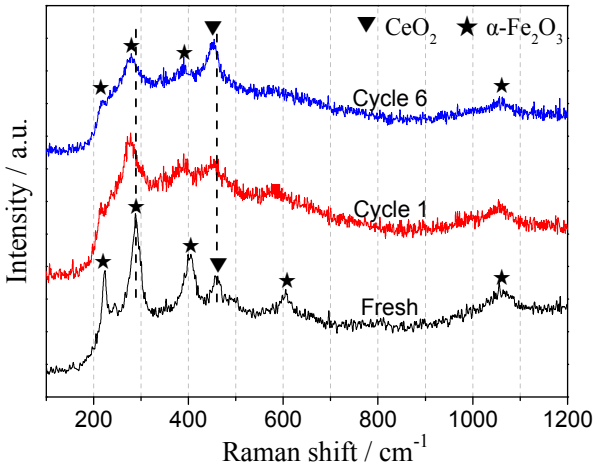

Figure 11. Effect of redox treatment on the Raman spectra of Ce20/Fe80 sample.